metabolites

MDPI

Article

Integrated Metabolic Profiling of Gallbladder Cancer Reveals Targetable Vulnerabilities and an Uncoupled Glycerol-3-Phosphate Shuttle Linked to Metastasis

Yuren Pan [1,†], Chak Lam Chan [1,†], Kaili Liu [1,†], Zhenyun Guo [2], Ying Zhu [1], Nan Wang [3], Da Xu [1,*] and Baobing Yin [1,2,*]

[1] Hepatobiliary Surgery, Department of General Surgery, Huashan Hospital & Cancer Metastasis Institute, Fudan University, Shanghai 200040, China; 24211220050@m.fudan.edu.cn (Y.P.); 26111280001@m.fudan.edu.cn (C.L.C.); 9159@huashan.org.cn (K.L.); yzhu14@fudan.edu.cn (Y.Z.)
[2] Department of Hepatopancreatobiliary Surgery, National Medical Center, Binhai Campus of the First Affiliated Hospital, Fujian Medical University, Fuzhou 350212, China; guozy@fjmu.edu.cn
[3] Department of Laboratory Medicine, Huashan Hospital, Fudan University, Shanghai 200040, China; b2026001095@student.pumc.edu.cn
* Correspondence: 10301010127@fudan.edu.cn (D.X.); yinbaobing@huashan.org.cn (B.Y.)
† These authors contributed equally to this work.

Abstract

Background: Gallbladder cancer (GBC) is an aggressive biliary tract malignancy with few targeted therapies. Though efforts have been made to identify actionable alterations and potential targeted strategies for GBC, its metabolic landscape and dependencies remain incompletely defined. **Methods**: We performed untargeted metabolomic profiling of 27 paired GBC tissues and adjacent nontumor tissues and integrated these data with public transcriptomic cohorts and DepMap CRISPR dependency data to characterize metabolic alterations and vulnerabilities in GBC. Additionally, we analyzed a single-cell RNA-sequencing (scRNA-seq) dataset to elucidate the potential biological role of glycerol-3-phosphate dehydrogenase 2 (GPD2). **Results**: The multi-omic integration revealed obvious metabolic remodeling in GBC, including enhanced lipid biosynthesis and hexosamine biosynthetic pathway activity within the carbon metabolic network, together with polyamine accumulation. The DepMap-based dependency analysis prioritized solute carrier family 7 member 5 (SLC7A5) and succinate dehydrogenase complex iron sulfur subunit B (SDHB) as clinically relevant metabolic vulnerabilities. Among all the metabolites, glycerol 3-phosphate (Gro3P) was the most depleted, in parallel with the accumulation of dihydroxyacetone phosphate (DHAP) and the reciprocal expression of glycerol-3-phosphate shuttle (G3PS) enzyme genes, which was correlated with poor overall survival. The functional experiments showed that GPD2 knockdown unexpectedly enhanced primary tumor growth in a subcutaneous xenograft model. However, the scRNA-seq analysis and the cell migration assays linked GPD2 to a metastasis-associated epithelial state and tumor-cell motility. **Conclusions**: This study characterizes the metabolic landscape of GBC and reveals an uncoupled G3PS marked by Gro3P depletion. GPD2 expression is associated with a metastasis-related malignant epithelial state and poor prognosis, while GPD2 knockdown reduces cell migration in vitro. These findings warrant the further investigation of GPD2 in GBC progression, but its role in metastatic dissemination and its therapeutic implications remain to be established.

Keywords: gallbladder cancer; metabolomics; metabolic reprogramming; glycerol-3-phosphate shuttle; GPD2

Check for updates

Received: 7 October 2026
Revised: 2 November 2026
Accepted: 16 November 2026
Published: 18 November 2026

Copyright: © 2026 by the authors. Licensee MDPI, Basel, Switzerland. This article is an open access article distributed under the terms and conditions of the Creative Commons Attribution (CC BY) license.

1. Introduction

Gallbladder cancer (GBC) is the most common biliary tract malignancy, characterized by late diagnosis, aggressive progression and high mortality [1]. Its incidence shows marked geographic variation, with the highest rates reported in the Andean regions of South America, Southeast Asia and East Asia [1–3]. Currently, surgical resection remains the only potentially curative treatment for early-stage GBC [1]. Since early GBC is usually asymptomatic, the majority of patients are diagnosed at an advanced stage, for whom durvalumab plus gemcitabine and cisplatin remains the first-line standard regimen, with a 5-year survival rate below 10% [4]. Despite efforts to identify actionable genomic alterations [5,6], effective targeted therapies are still lacking, and precision medicine strategies have not been established for this disease [7].

Metabolic reprogramming has been regarded as a core hallmark of tumor cells, enhancing their adaptability to cope with both endogenous insults, such as specific mutations, and exogenous challenges imposed by the complex tumor microenvironment (TME) [8]. These metabolic adaptations facilitate tumor growth, invasion and therapy resistance, but they can also generate metabolic liabilities that are amenable to therapeutic intervention. Such liabilities have been well defined in multiple tumor types [9–11], whereas the metabolic architecture and druggable metabolic dependencies of GBC remain poorly understood.

As one of the two major NADH shuttle systems, the glycerol-3-phosphate shuttle (G3PS) functions as a cyclical loop. Glycerol-3-phosphate dehydrogenase 1 (GPD1) reduces dihydroxyacetone phosphate (DHAP) to glycerol 3-phosphate (Gro3P) to regenerate NAD+, whereas glycerol-3-phosphate dehydrogenase 2 (GPD2) oxidizes Gro3P back to DHAP, concurrently transferring the NADH-derived electrons to the electron transport chain (ETC) [12]. Meanwhile, Gro3P and DHAP serve as the glycerol backbone for glycerolipids, glycerophospholipids and ether lipids. Thus, G3PS acts as a hub linking glycolysis, redox homeostasis and lipid biosynthesis.

Compared with the malate–aspartate shuttle (MAS), the role of G3PS in cancer remains less well characterized. Accumulating evidence has demonstrated that the expression patterns of GPD1 and GPD2 are frequently uncoupled in various human cancers, implying that tumor cells remodel glycerol lipid metabolism via this regulatory node [13,14]. However, the metabolic consequences of this uncoupling, its relevance to tumor progression and its therapeutic implications are incompletely resolved.

Here, we used untargeted metabolomic profiling of clinical GBC tissues to define the metabolic landscape of this malignancy. Combined with public RNA-sequencing datasets and DepMap CRISPR dependency data, we evaluated clinically relevant metabolic vulnerabilities in GBC. Our results revealed that Gro3P was the most significantly depleted metabolite in GBC tissues, and that this depletion was accompanied by an uncoupled G3PS pattern, with downregulation of *GPD1*/*GPD1L* and upregulation of *GPD2*. Further analyses showed that *GPD2* was highly expressed in an aggressive malignant epithelial phenotype and was associated with tumor metastasis. These findings support further investigation of GPD2 in GBC biology and its potential therapeutic relevance.

2. Materials and Methods

2.1. Untargeted Metabolomics Profiling

Tissue samples (20 mg) were homogenized (30 Hz, 20 s) and extracted using a precooled methanol:water solution (7:3, *v*/*v*; 400 µL) containing internal standards (Table S1). Following shaking (1500 rpm, 5 min) and incubation (on ice, 15 min), the mixture was centrifuged (12,000 rpm, 10 min, 4 °C). The supernatant was further incubated (−20 °C, 30 min) and centrifuged again (12,000 rpm, 3 min) prior to LC-MS analysis. Chromatographic separation was achieved using an ACQUITY BEH C18 column (Waters, Milford,

MA, USA; 1.7 µm, 2.1 mm × 100 mm) for both positive and negative ionization modes, and an ACQUITY BEH HILIC column (Waters; 1.7 µm, 2.1 mm × 150 mm) for polar metabolite analysis in negative mode. The C18 and HILIC separations provided complementary coverage of less polar and highly polar metabolites, respectively, while the use of both ionization polarities further broadened metabolite coverage. Mass spectrometry was performed on a TripleTOF 5600+ system (Sciex, Framingham, MA, USA) in Information-Dependent Acquisition (IDA) mode. Source parameters, including temperature (550 °C) and ion spray voltages (5000 V for positive mode and −4000 V for negative mode), were maintained. TOF-MS and product ion scans were conducted across defined mass ranges (50–1000 Da and 25–1000 Da, respectively), with candidate ions (top 18 per cycle) monitored for structural identification. Six independent pooled quality control (QC) samples were prepared, each by combining equal aliquots from all study samples. These QC samples were injected at evenly spaced positions throughout the analytical sequence and analyzed under identical chromatographic and mass spectrometric conditions. Metabolite annotations meeting the acceptance criteria from the three analytical conditions were combined into the final dataset presented in Table S1.

2.2. Cell Lines

Human GBC cell lines (GBC-SD, NOZ and OCUG-1) and the immortalized human gallbladder epithelial cell line L-2F7 were generous gifts from Prof. Yingbin Liu's laboratory (Renji Hospital, Shanghai, China), while the TGBC1TKB cell line was purchased from RIKEN BioResource Research Center (Tsukuba, Japan; RCB1129). GBC cells were cultured in DMEM medium (Thermo Fisher, Waltham, MA, USA; 11965092), supplemented with 10% FBS (Thermo Fisher; A5256701) and 1% penicillin/streptomycin (Thermo Fisher; 15140-122). L-2F7 cells were cultured following the conditions described in the original publication [15]. All cell lines were maintained at 37 °C in a humidified atmosphere containing 5% CO_2. All cell lines were authenticated by Short Tandem Repeat (STR) profiling and were confirmed to be free of mycoplasma contamination before use.

2.3. Lentiviral Transduction

To establish stable GPD2-knockdown or -overexpression cell lines, cells were transduced with lentiviral vectors containing either a short hairpin RNA (shRNA) targeting GPD2 (sh-GPD2), a GPD2-overexpression sequence (OE-GPD2), or their corresponding negative controls (shCtrl or empty Vector). Transductions were performed at an appropriate multiplicity of infection (MOI) in the presence of polybrene (8 µg/mL). After 48 h, transduced cells were selected using puromycin in the culture medium for at least 72 h. The efficiency of knockdown and overexpression was confirmed by quantitative real-time PCR (qPCR) and Western blot analysis.

2.4. Western Blot

Adherent cells were harvested when they reached 70–80% confluence. Briefly, cells were washed twice with pre-cooled phosphate-buffered saline (PBS) and lysed in RIPA lysis buffer (Beyotime, Shanghai, China; P0013C) supplemented with protease and phosphatase inhibitors (Beyotime; P1046) for 30 min on ice. For tissue samples, they were homogenized using a tissue homogenizer in the presence of RIPA buffer. The resulting lysates were centrifuged (12,000 rpm, 15 min, 4 °C) to collect the supernatant. Protein samples were mixed with loading buffer and denatured (95 °C, 10 min). Equal amounts of protein were separated by 10% SDS-PAGE and subsequently transferred onto PVDF membranes (Millipore, Burlington, MA, USA; IPVH00010). After blocking with non-fat milk (5%; 1 h, room temperature), the membranes were incubated with primary antibodies

overnight at 4 °C. Following incubation with HRP-conjugated secondary antibodies (1 h, room temperature), protein bands were visualized using an enhanced chemiluminescence (ECL) kit and captured using an imaging system.

2.5. Immunohistochemistry (IHC) and Evaluation

Immunohistochemistry was performed on tissue microarray (TMA) sections. After deparaffinization and rehydration, antigen retrieval was performed by microwave heating in citrate buffer (pH 6.0) for 15 min. Endogenous peroxidase and non-specific binding were blocked with 3% H_2O_2 (10 min) and 5% normal goat serum (30 min, room temperature), respectively. Sections were then incubated with the primary antibody overnight at 4 °C, followed by an HRP-conjugated secondary antibody (30 min, room temperature), visualized with a DAB substrate kit, and counterstained with hematoxylin. Staining was independently scored by two senior pathologists blinded to the clinicopathological data.

The immunoreactive score (IRS) was calculated as staining intensity (SI) × percentage of positive cells (PP). SI was graded as 0 (negative), 1 (weak), 2 (moderate), or 3 (strong); PP as 0 (<5%), 1 (5–25%), 2 (26–50%), 3 (51–75%), or 4 (>75%). The resulting IRS (0–12) stratified samples into low- (0–6) and high- (7–12) expression groups for subsequent analysis.

2.6. Cell Viability Assays

Cell viability was evaluated using a Cell Counting Kit-8 (CCK-8; Dojindo, Mashiki, Kumamoto, Japan; CK04). Cells were seeded into 96-well plates (3×10^3 cells/well) and incubated for 12 h to allow for attachment. At each 24 h interval, CCK-8 solution (10 µL/well) was added to the culture medium. After incubation (37 °C, 2 h), the absorbance at 450 nm was measured using a microplate reader (BioTek, Winooski, VT, USA; Synergy Neo2). Cell growth curves were constructed by plotting the absorbance values against time.

2.7. Migration Assays

Cell migration capacity was evaluated using 24-well Transwell chambers with 8-µm pore size inserts (Corning, Tewksbury, MA, USA; 3422). Briefly, GBC-SD cells (3×10^4 cells/well) were harvested, resuspended in 200 µL of serum-free DMEM medium, and seeded into the upper chamber. The lower chamber was filled with 600 µL of complete culture medium supplemented with 10% FBS. After incubation at 37 °C for 24 h, cells remaining on the upper surface of the membrane were carefully removed using a cotton swab. The migrated cells on the lower surface of the membrane were fixed with 4% paraformaldehyde for 15 min and subsequently stained with 0.1% crystal violet solution for 20 min at room temperature. For quantification, images of four random fields of view were captured for each well using an inverted microscope. The number of migrated cells was counted manually, and the average count across the four fields was calculated to represent each well. All assays were performed in three independent biological replicates.

2.8. In Vivo Xenograft Model

For the in vivo study, 6-week-old female BALB/c nude mice were randomly assigned to three experimental groups ($n = 6$). GBC-SD cells (2×10^6 cells per injection) were resuspended in 100 µL of a cold mixture of PBS and Matrigel (Corning; 356234) at a 1:1 ratio to ensure optimal engraftment and then injected subcutaneously into the right flank of each mouse. Tumor formation was monitored starting from day 4 post-grafting, with tumor length (L) and width (W) measured every 4 days using a digital caliper. Tumor volume (V) was calculated using the formula $V = (L \times W^2)/2$. The observation period lasted for 28 days, after which the mice were humanely sacrificed for subsequent analysis.

2.9. Metabolomic Data Processing and Statistical Analysis

2.9.1. Orthogonal Partial Least Squares-Discriminant Analysis (OPLS–DA)

OPLS–DA was performed using the *ropls* R package (version 1.44.0) on $\log_2$-transformed, unit-variance-scaled metabolite intensities, with one predictive and two orthogonal components, to discriminate tumor ($n = 27$) from matched adjacent non-tumor samples ($n = 27$). Model performance was assessed by predictive R^2X, orthogonal R^2X, R^2Y, and 7-fold cross-validated Q^2; significance and overfitting were evaluated by 200-iteration permutation testing ($pR^2Y = 0.02$, $pQ^2 = 0.005$). Score plots with 95% confidence ellipses were generated in *ggplot2* (version 4.0.4).

2.9.2. Univariate Differential Metabolite Analysis

Raw peak areas were normalized by total ion current (TIC) per sample and $\log_2$-transformed. Differential metabolites between GBC tumor and matched adjacent non-tumor tissues were identified by paired Student's *t*-test, with *p* values adjusted by the Benjamini–Hochberg procedure to control the false discovery rate (FDR). Variable importance in projection (VIP) scores were derived from the OPLS–DA model described above. Metabolites with FDR < 0.05 and VIP > 1 were defined as significantly differential. Log_2 fold change was calculated as $\text{mean}(\log_2(\text{tumor})) - \text{mean}(\log_2(\text{adjacent}))$.

2.9.3. KEGG Pathway Enrichment

Differential metabolites with valid KEGG Compound IDs were mapped to KEGG *Homo sapiens* metabolic pathways (global overview maps such as hsa01100 and hsa01110 were excluded). For each pathway, K denotes the total number of detected metabolites mapped to the pathway, k the number of differential metabolites mapped to the pathway (k = k_up + k_down). Over-representation was tested by hypergeometric test against all KEGG-annotated detected metabolites as the assay-specific background, with Benjamini–Hochberg FDR correction. Pathways with $K \geq 3$ and $k \geq 1$ were retained; the differential abundance (DA) score was calculated as $(k_up - k_down)/k$, and the Rich Factor as k/K. Pathways with $k \geq 3$ are visualized in Figure 1G.

2.9.4. Metabolite Set Enrichment Analysis (MSEA)

MSEA was performed using the *clusterProfiler* R package (version 4.20.3) on metabolites with valid KEGG Compound IDs. Metabolites were ranked by the paired Student's *t*-statistic between GBC tumor and matched adjacent non-tumor samples, computed on $\log_2$-transformed, TIC-normalized intensities. Pathway annotations were restricted to KEGG *Homo sapiens* metabolic pathways. Normalized enrichment scores (NES) and permutation-based *p* values were computed, with multiple testing correction by the Benjamini–Hochberg procedure. Pathways with $|NES| > 1.5$ and Benjamini–Hochberg-adjusted $p < 0.05$ were considered significantly enriched.

2.10. Analysis of Public Transcriptomic Data

For the datasets (GSE62335, GSE76633, GSE100363, GSE138109, GSE139682 and GSE202479) from the Gene Expression Omnibus (GEO) database (58 tumor tissue samples; 51 normal tissue samples), they were combined using the Rank-in normalization method to harmonize cross-platform data and mitigate inter-study batch effects [16]. The complete list of identified DEGs is provided in Table S2. For the Fu-GBC datasets [17], transcripts per million (TPM) normalized expression values were mined from the Supplementary Materials of the research article.

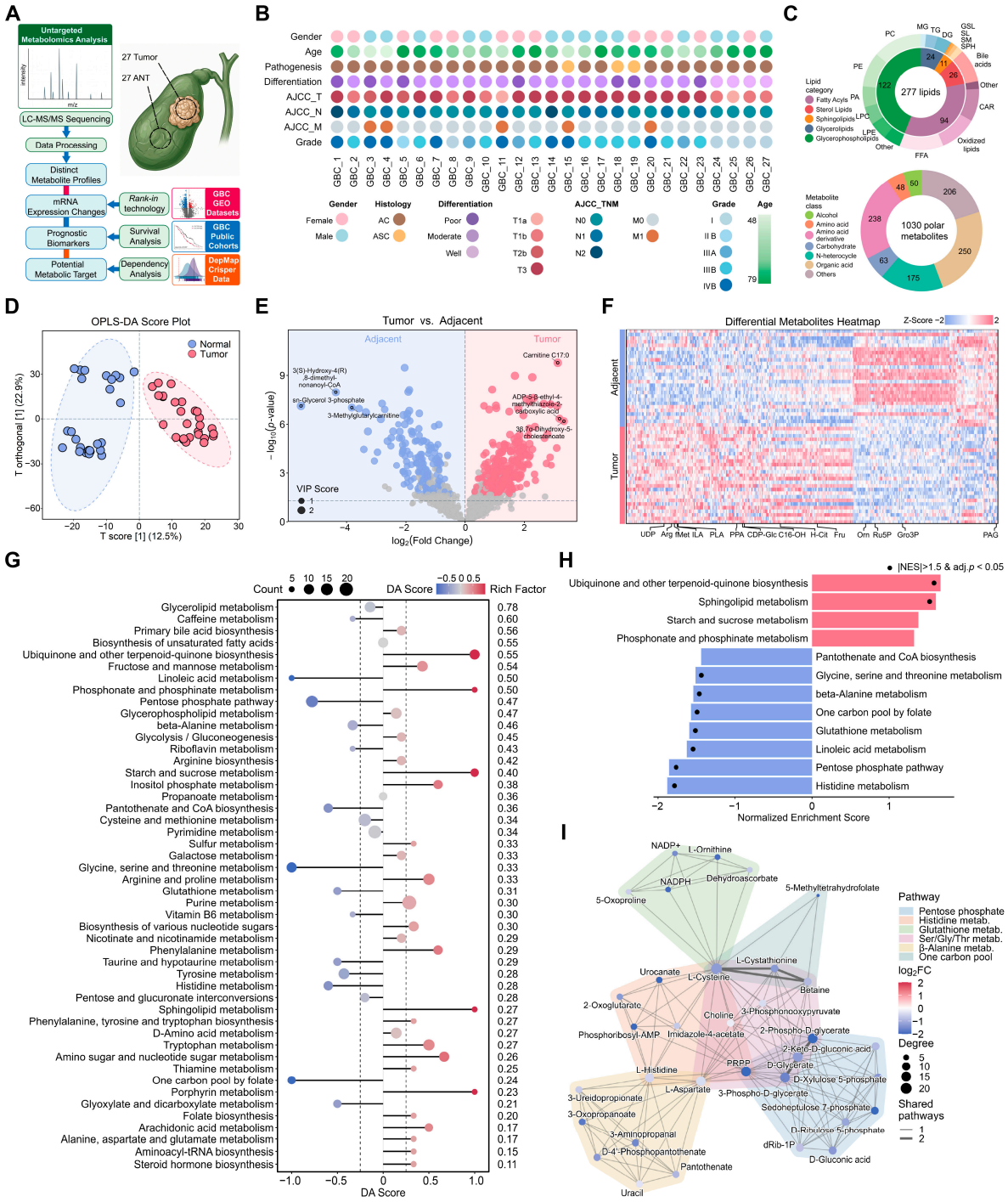


Figure 1. Untargeted metabolomic profiling of gallbladder cancer. (**A**) Schematic of this study's design; (**B**) clinicopathological characteristics of the 27-patient GBC cohort. Each column represents one patient; (**C**) composition of detected metabolites: 277 lipid species (top) classified by lipid category and 1030 polar metabolites (bottom) classified by metabolite class; (**D**) orthogonal partial least squares–discriminant analysis (OPLS–DA) score plot showing clear separation between tumor and adjacent nontumor tissue samples; (**E**) volcano plot of paired Student's *t*-test with OPLS–DA VIP filtering (FDR < 0.05, VIP > 1). Representative metabolites with the largest changes in each direction are labeled; (**F**) heatmap of all differential metabolites, with row-wise *z*-score-normalized intensities. Selected metabolites are labeled along the bottom axis; (**G**) KEGG DA-score lollipop for 48 metabolism pathways with ≥3 differential metabolites; (**H**) pre-ranked metabolite set enrichment analysis (MSEA) showing the top up- and downregulated KEGG pathways ranked by |NES|; (**I**) metabolite–metabolite interaction network of the six interconnected downregulated pathways. *PC*,

https://doi.org/10.3390/metabo16110904

phosphatidylcholine; *PE*, *phosphatidylethanolamine*; *PA*, *phosphatidic acid*; *LPC*, *lysophosphatidylcholine*; *LPE*, *lysophosphatidylethanolamine*; *FFA*, *free fatty acid*; *CAR*, *acylcarnitine*; *SPH*, *sphingoid bases*; *SM*, *sphingomyelin*; *SL*, *sulfatide*; *GSL*, *glycosphingolipid*; *DG*, *diacylglycerol*; *MG*, *monoacylglycerol*; *TG*, *triacylglycerol*. *UDP*, *uridine 5′-diphosphate*; *Arg*, *arginine*; *fMet*, *N-formylmethionine*; *ILA*, *indole-3-lactic acid*; *PLA*, *L-3-phenyllactic acid*; *PPA*, *phenylpyruvic acid*; *CDP-Glc*, *CDP-glucose*; *C16-OH*, *carnitine C16-OH*; *H-Cit*, *homocitrulline*; *Fru*, *D-fructose*; *Orn*, *ornithine*; *Ru5P*, *D-ribulose 5-phosphate*; *PAG*, *phenylacetylglutamine*.

2.11. Public Single-Cell RNA-Sequencing Data Analysis

2.11.1. Patient-Level Epithelial GPD2 Stratification and Survival Analysis

From the Supplementary Materials of Zhou et al. [18], single-cell RNA-sequencing data of primary tumor adenocarcinoma malignant epithelium from 86 gallbladder cancer patients with matched survival information were obtained. The mean log-normalized *GPD2* expression per patient was used to stratify patients at the upper quartile into epi-GPD2-high and epi-GPD2-low groups, and overall survival was compared by Kaplan–Meier analysis with log-rank test (R packages *survival*, version 3.8-12, and *survminer*, version 0.5.2).

2.11.2. Single-Cell Visualization of Malignant Epithelium Subpopulations

Single-cell RNA-sequencing data of malignant epithelial cells from primary adenocarcinoma gallbladder cancers were obtained from Zhou et al. Per-sample doublets were identified with *scDblFinder* (version 1.26.9), and cells were retained based on the criteria 500 < nFeature_RNA < 6500; 1000 < nCount_RNA < 25,000; dissociation stress score < 2.5, and singlet classification. Filtered counts were log-normalized in *Seurat* (version 5.6.0) (scale factor 1×10^4), 2000 highly variable genes were identified by the variance-stabilizing transformation, and the first 40 principal components were corrected for sample-level batch effects using *Harmony* ($\theta = 4$) (version 2.0.5). Cells were clustered by the Louvain algorithm at resolution 0.5 and embedded by UMAP (min.dist = 0.3; n.neighbors = 30). On the same embedding, *GPD2* expression density was visualized with *Nebulosa* (version 1.22.0), the metabolism-associated GM16 module previously defined by Zhou et al. was overlaid using the authors' original cell annotations, and cells were classified as P_Mets (primary tumors with documented distant metastasis) versus P (without) and visualized by group.

3. Results

3.1. Untargeted Metabolomics Characterizes Global Metabolic Reprogramming in GBC

To investigate metabolic features and candidate vulnerabilities in GBC, we collected primary tumor tissues from 27 patients, including 3 adenosquamous carcinomas (ASCs) and 24 adenocarcinomas (ACs), together with 27 patient-matched adjacent nontumor tissues (ANT) as controls (Figure 1A,B). All samples were subjected to untargeted metabolomic profiling, and clinicopathological features of the cohort are summarized in Figure 1B.

After excluding exogenous compounds (e.g., medications and environmental contaminants), 1030 polar metabolites and 277 lipid species were retained for downstream analysis (Figure 1C and Table S1). Orthogonal partial least squares-discriminant analysis (OPLS–DA) showed clear separation between GBC and ANT samples along the predictive and orthogonal components ($R^2X = 0.411$, $R^2Y = 0.877$, $Q^2 = 0.732$), indicating profound metabolic differences between tumor and nontumor tissues (Figure 1D).

Paired differential metabolite analysis identified a tumor-associated metabolic signature that distinguished GBC from ANT samples (Figure 1E,F). Several metabolites were markedly depleted in GBC tissues, including sn-glycerol 3-phosphate (Gro3P), 3-methylglutarylcarnitine, and 3(S)-hydroxy-4(R),8-dimethyl-nonanoyl-CoA. In contrast, carnitine C17:0, ADP-5-β-ethyl-4-methylthiazole-2-carboxylic acid, and 3β,7α-dihydroxy-5-cholestenoate were enriched in tumors (Figure 1E,F).

Given that different cancer types exhibit distinct metabolic patterns [19–21], we reasoned that GBC harbors unique metabolic rewiring and specific pathway vulnerabilities. To further elucidate the biological significance of these metabolic shifts, we performed pathway enrichment analysis of the metabolites. KEGG pathway enrichment combined with differential abundance (DA) score (Figure 1G) showed that several core metabolic pathways presented an overall trend of metabolite depletion in GBC. Although glycerolipid metabolism had the highest coverage of differential metabolites (Rich Factor = 0.78), its DA score was close to zero, indicating bidirectional changes rather than consistent downregulation. By comparison, the pentose phosphate pathway, glycine, serine and threonine metabolism, one carbon pool by folate, linoleic acid metabolism and histidine metabolism showed the most prominent metabolite depletion. As a threshold-free analysis, rank-based Metabolite Set Enrichment Analysis (MSEA) identified histidine metabolism (NES = −1.88, adj.$p = 3.2 \times 10^{-3}$) and the pentose phosphate pathway (NES = −1.86, adj.$p = 6.0 \times 10^{-3}$) as the most significantly downregulated pathways, accompanied by linoleic acid metabolism (NES = −1.62, adj.$p = 0.023$), glutathione metabolism (NES = −1.59, adj.$p = 0.029$), one carbon pool by folate (NES = −1.57, adj.$p = 0.033$), β-alanine metabolism (NES = −1.54, adj.$p = 0.036$) and glycine, serine and threonine metabolism (NES = −1.51, adj.$p = 0.039$), while ubiquinone and other terpenoid-quinone biosynthesis (NES = 1.67, adj.$p = 0.016$) and sphingolipid metabolism (NES = 1.61, adj.$p = 0.023$) emerged as the top upregulated pathways (Figure 1H).

To clarify the crosstalk among these pathways via shared metabolites, we constructed an interaction network using leading-edge metabolites from the significantly downregulated pathways identified by MSEA (Figure 1I). The resulting network revealed a tightly interconnected module spanning six pathways: the pentose phosphate pathway (PPP), histidine, glutathione (GSH), one-carbon folate, glycine/serine/threonine (Gly/Ser/Thr), and β-alanine metabolism. This module was centered on L-cysteine (L-Cys) and phosphoribosyl pyrophosphate (PRPP). L-Cys emerged as the most highly shared hub metabolite, simultaneously appearing in the leading edges of histidine metabolism, GSH metabolism, one-carbon folate metabolism, and Gly/Ser/Thr metabolism. PRPP linked the PPP and histidine metabolism pathways. Other key hub metabolites, including L-cystathionine, 3-phospho-D-glycerate (3-PG), 2-phospho-D-glycerate (2-PG), D-xylulose-5-phosphate (Xu5P), and 5-methyltetrahydrofolate (5-MTHF), further strengthened the connectivity of this metabolic network. According to canonical biochemical routes, the module encompasses precursor pools feeding three interlinked functional outputs: de novo nucleotide biosynthesis (PRPP and Xu5P via the PPP; 3-PG/2-PG via the Ser/Gly–one-carbon axis), GSH-mediated redox homeostasis (L-Cys as the rate-limiting GSH precursor, with L-cystathionine supplying cysteine via transsulfuration), and one-carbon–dependent methylation (5-MTHF as the proximal methyl donor of the methionine cycle, with Ser and Gly providing one-carbon units).

Although steady-state metabolite abundance cannot directly reflect metabolic flux, the coordinated depletion of these interconnected precursor pools is most parsimoniously interpreted as evidence of heightened substrate consumption rather than reduced biosynthetic activity [22]. The three downstream functional outputs, including nucleotide biosynthesis, GSH-dependent redox homeostasis and methyl group metabolism, meet the core anabolic and protective requirements of proliferating tumor cells [23].

Collectively, our metabolomic profiling defines a unique metabolic landscape of GBC: profound depletion of Gro3P together with selected acyl-CoA and acylcarnitine species, coordinated downregulation of a six-pathway module that sustains nucleotide synthesis, redox balance, and methylation, and concurrent activation of ubiquinone biosynthesis and sphingolipid metabolism.

3.2. Integrated Analysis Reveals Metabolic Alterations of Glycosylation and Lipid Biosynthesis in GBC

To connect metabolite alterations with potential molecular drivers, we integrated the metabolomic data with public transcriptomic datasets from the Gene Expression Omnibus (GEO) (Table S2) and cross-validated the findings using transcriptomic data from the Fu-GBC cohort [17]. Mapping differentially expressed genes encoding metabolic enzymes to corresponding metabolic nodes suggested potential rewiring of carbon metabolism in GBC tissues (Figure 2A).

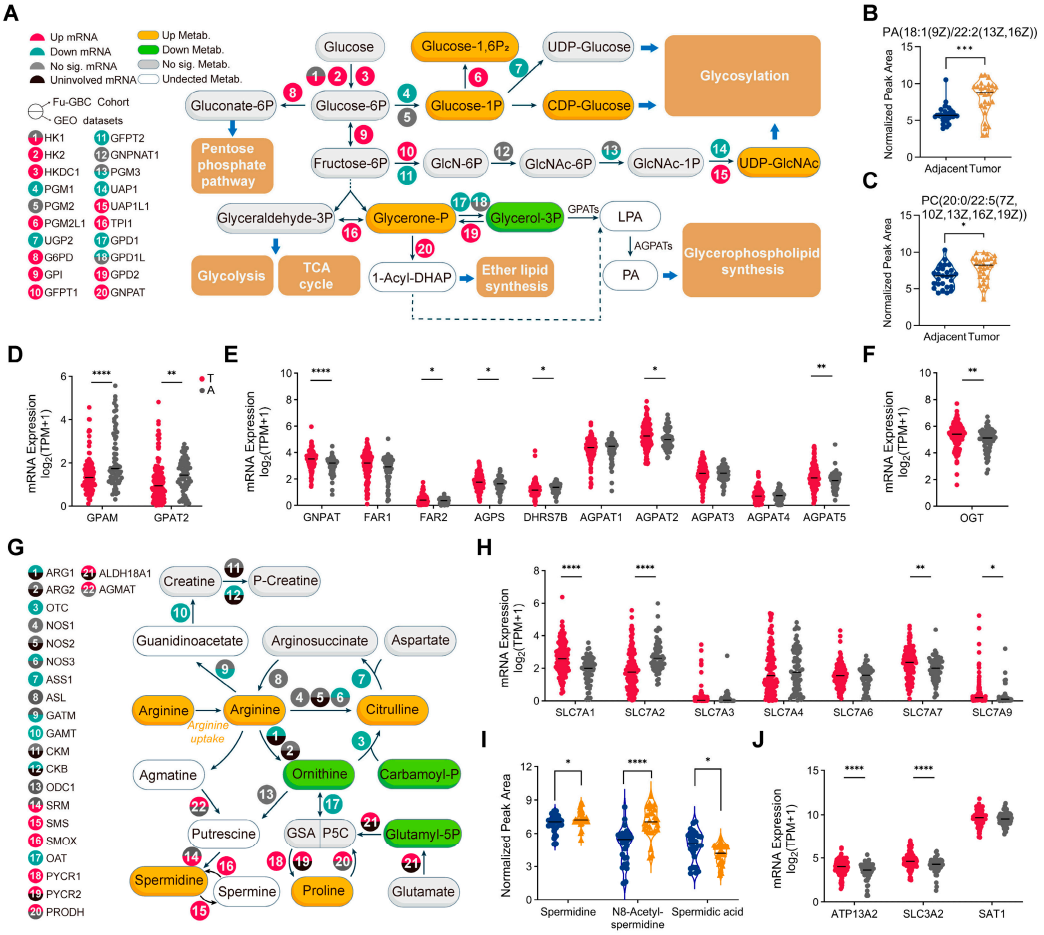


Figure 2. Integrated transcriptomic–metabolomic alterations in central carbon metabolism and arginine–polyamine metabolism in GBC. (**A**) Integrated pathway map of central carbon metabolism, spanning glycolysis, the pentose phosphate pathway, the hexosamine biosynthetic pathway (HBP), glycerophospholipid and ether–lipid synthesis. Metabolite changes (untargeted metabolomics; GBC tumor versus adjacent) and enzyme transcript changes (Fu-GBC cohort and GEO datasets) are overlaid, with the direction of change indicated by the color key. Numbered enzyme genes are listed at left; (**B**,**C**) normalized peak areas of representative glycerophospholipid species, PA(18:1/22:2) and PC(20:0/22:5), in adjacent and tumor tissues; (**D**,**E**) transcript levels in tumor (T) versus adjacent (A) tissues for (**D**) the Gro3P-acylating enzymes *GPAM* and *GPAT2* and (**E**) ether–lipid biosynthetic enzymes together with the AGPAT family; (**F**) transcript level of *OGT* in tumor versus adjacent tissues; (**G**) integrated pathway map of arginine, urea-cycle, polyamine, and proline metabolism, overlaid with metabolite and enzyme transcript changes as in (**A**); (**H**) transcript levels of cationic and SLC7-family amino-acid transporters in tumor versus adjacent tissues; (**I**) normalized peak areas of spermidine, N^8-acetylspermidine, and spermidic acid (CEGABA) in adjacent and tumor tissues; (**J**) transcript levels of *ATP13A2*, *SLC3A2*, and *SAT1* in tumor versus adjacent tissues. Metabolite comparisons (**B**,**C**,**I**) were analyzed by a paired Student's *t* test; transcript comparisons (**D**–**F**,**H**,**J**) were

analyzed by a two-sided Mann–Whitney *U* test. * $p < 0.05$; ** $p < 0.01$; *** $p < 0.001$; **** $p < 0.0001$. *CEGABA*, *N-carboxyethyl-γ-aminobutyric acid*; *LPA*, *lysophosphatidic acid*; *PA*, *phosphatidic acid*; *TPM*, *transcripts per million*.

The transcripts encoding the glycolytic enzymes HK1, HK2, HKDC1, and GPI were consistently increased in GBC (Figure 2A). However, downstream carbon metabolism diverged at the DHAP/Gro3P node, where DHAP accumulated while Gro3P was markedly depleted. This imbalance was accompanied by a reciprocal enzyme-expression pattern: the Gro3P-producing enzyme genes *GPD1* and *GPD1L* were downregulated, whereas the mitochondrial Gro3P-consuming enzyme gene *GPD2* was overexpressed (Figure 2A).

Gro3P and its redox partner DHAP sit at a branchpoint between glycerophospholipid and ether–lipid biosynthesis. Gro3P can be acylated to lysophosphatidic acid (LPA) by the GPAT family and subsequently to phosphatidic acid (PA) by AGPAT enzymes, providing the core route into glycerophospholipid synthesis; consistent with selective remodeling at this node, specific glycerophospholipid species accumulated in tumors (Figure 2B,C). However, GPAM (GPAT1) and GPAT2 transcripts were significantly reduced (Figure 2D), while the consequences for flux through the conventional Gro3P-to-LPA pathway remain undetermined. We therefore examined the alternative, DHAP-dependent ether–lipid route, in which GNPAT acylates DHAP and AGPS, together with the fatty-alcohol–generating reductases FAR1 and FAR2, commits the backbone to ether–linked lipids. Several of these ether–lipid biosynthetic enzyme genes, including *GNPAT*, *AGPS* and *FAR2*, were upregulated in GBC (Figure 2E). Together with increased *GPD2* and reduced *GPD1*/*GPD1L* transcript abundance (Figure 2A), this enzyme-expression pattern suggests that the DHAP/Gro3P pool may be preferentially channeled toward ether–lipid biosynthesis rather than conventional glycerophospholipid synthesis. This interpretation is consistent with the established GPD2–DHAP–ether–lipid axis that promotes tumor progression independently of GPD2's bioenergetic role [24], and with the observation that GPD1L repression elevates DHAP-derived ether–lipid synthesis [25]. Ether lipids may in turn influence membrane fluidity and ferroptosis susceptibility [26–28].

In addition to lipid remodeling, GBC tissues exhibited alterations in metabolites and enzyme gene expression associated with the hexosamine biosynthetic pathway (HBP). UDP-GlcNAc, the terminal HBP product and a major donor for protein O-GlcNAcylation [29], was increased in GBC tissues relative to adjacent controls (Figure 2A). Although the canonical terminal enzyme gene *UAP1* was downregulated, *UAP1L1* was strongly overexpressed, a pattern compatible with maintained UDP-GlcNAc supply but warranting further biochemical confirmation. The expression of *OGT*, which uses UDP-GlcNAc to modify target proteins, was also increased in GBC (Figure 2F). These findings identify alterations in the HBP–OGT axis that warrant further investigation of UDP-GlcNAc synthesis and protein O-GlcNAcylation in GBC.

3.3. Enhanced Amino Acid Transport Fuels Reprogrammed Arginine and Polyamine Metabolism in GBC

We next explored amino acid metabolic reprogramming in GBC and observed substantial remodeling of the urea cycle and polyamine biosynthetic pathway (Figure 2G). Metabolomic analysis revealed accumulation of arginine and citrulline in tumor tissues. Despite abundant arginine, the endogenous urea cycle appeared suppressed, as evidenced by ornithine depletion and coordinated downregulation of key urea-cycle enzyme genes, including *ARG1*, *OTC* and *ASS1* (Figure 2G).

Given this suppression of endogenous arginine metabolism, we hypothesized that increased extracellular arginine uptake contributes to its intracellular accumulation. Transcriptomic analysis confirmed the upregulation of *SLC7A1* (*CAT1*), a major arginine transporter,

in GBC tissues (Figure 2H). Other members of the SLC7 family, such as *SLC7A7* and *SLC7A9*, as well as the essential chaperone *SLC3A2*, were also upregulated (Figure 2H,J) [30]. These data indicate that enhanced amino acid transport enables GBC cells to maintain sufficient intracellular arginine despite reduced urea cycle activity.

Ornithine depletion in the presence of abundant arginine implied rapid consumption of this intermediate by downstream metabolic pathways (Figure 2G). We therefore examined two major metabolic fates of ornithine: polyamine biosynthesis, a pathway frequently dysregulated in cancer [31], and the proline cycle. GBC tissues showed accumulation of spermidine and N^8-acetylspermidine, along with reduced spermidic acid, suggesting remodeling of the spermidine-associated polyamine pool rather than simple activation of a linear polyamine biosynthetic pathway (Figure 2I). Meanwhile, upregulation of *ATP13A2* [32], which encodes a lysosomal polyamine exporter, together with a parallel trend toward increased *SAT1*, which encodes the key polyamine acetyltransferase SSAT [33], further suggested enhanced polyamine transport, acetylation, and turnover in GBC (Figure 2J). By contrast, the ornithine-to-proline metabolic branch appeared attenuated, as *OAT* was downregulated, whereas *ALDH18A1* and *PYCR1/2* were upregulated, suggesting that proline metabolism may be mainly sustained by glutamate-derived substrates instead of ornithine. Collectively, these findings identify alterations in arginine-, ornithine-, polyamine-, and proline-associated metabolite abundances and gene expression in GBC, while the underlying metabolic fluxes remain to be established.

3.4. Integrated CRISPR Dependency and Clinical Profiling Identifies Metabolic Dependencies in GBC

To identify metabolic targets with therapeutic potential, we characterized gene dependencies in GBC cell lines using the DepMap CRISPR database and integrated these results with Fu-GBC cohort data to assess clinical relevance. To focus on cancer-selective rather than pan-essential dependencies, we first excluded the 1827 common essential genes annotated by DepMap from the analytic gene set. Within this filtered gene space, metabolic genes were annotated based on a curated set ($n = 2851$) built upon the Human-GEM genome-scale metabolic reconstruction (Table S3) [34]. By comparing mean gene expression with dependency scores across GBC models, we identified a subset of metabolic genes required for GBC cell viability, including *ATIC*, *UMPS*, *SREBF1*, and *SCAP* (Figure 3A).

To prioritize candidates with both functional and clinical relevance, we applied two criteria: (i) a stringent DepMap dependency threshold of mean Gene Effect < -0.5 across the six GBC cell lines (the convention for selectively essential genes), and (ii) elevated tumor expression in the Fu-GBC bulk transcriptomic cohort (fold change > 1.0 versus paired adjacent tissues). Metabolic genes satisfying both criteria included *SCAP*, *SREBF1*, *TYMS* and *ATIC* (Figure 3B). Notably, most metabolic genes with strong GBC-selective dependency were concomitantly upregulated in tumor tissues (Figure 3B, upper portion). This phenomenon suggests that GBC cells frequently upregulate the metabolic enzymes on which they rely for survival, a hallmark of non-oncogenic metabolic addiction [35,36].

These dependency-associated genes spanned five metabolic programs: lipogenesis initiation, phospholipid synthesis, de novo pyrimidine synthesis, de novo purine synthesis, and the hexosamine biosynthetic pathway (Figure 3C). Representative genes within each module exhibited stronger dependency profiles in GBC cell lines than in other cancer models: *SCAP*, *SREBF1*, and *MBTPS1* in lipogenesis initiation; *PCYT1A* and *PTDSS1* in phospholipid synthesis; *CAD* in de novo pyrimidine synthesis; *PFAS* and *ATIC* in de novo purine synthesis; and *GFPT1* and *GNPNAT1* in the HBP module (Figure 3D). Notably, the HBP dependency converged with our preceding metabolomic and transcriptomic analyses, which showed UDP-GlcNAc accumulation and elevated expression of *UAP1L1* and OGT in GBC tissues.

Together, these multi-omic lines of evidence converge on the HBP–O-GlcNAcylation axis as both a metabolic hallmark and a functional requirement in GBC.

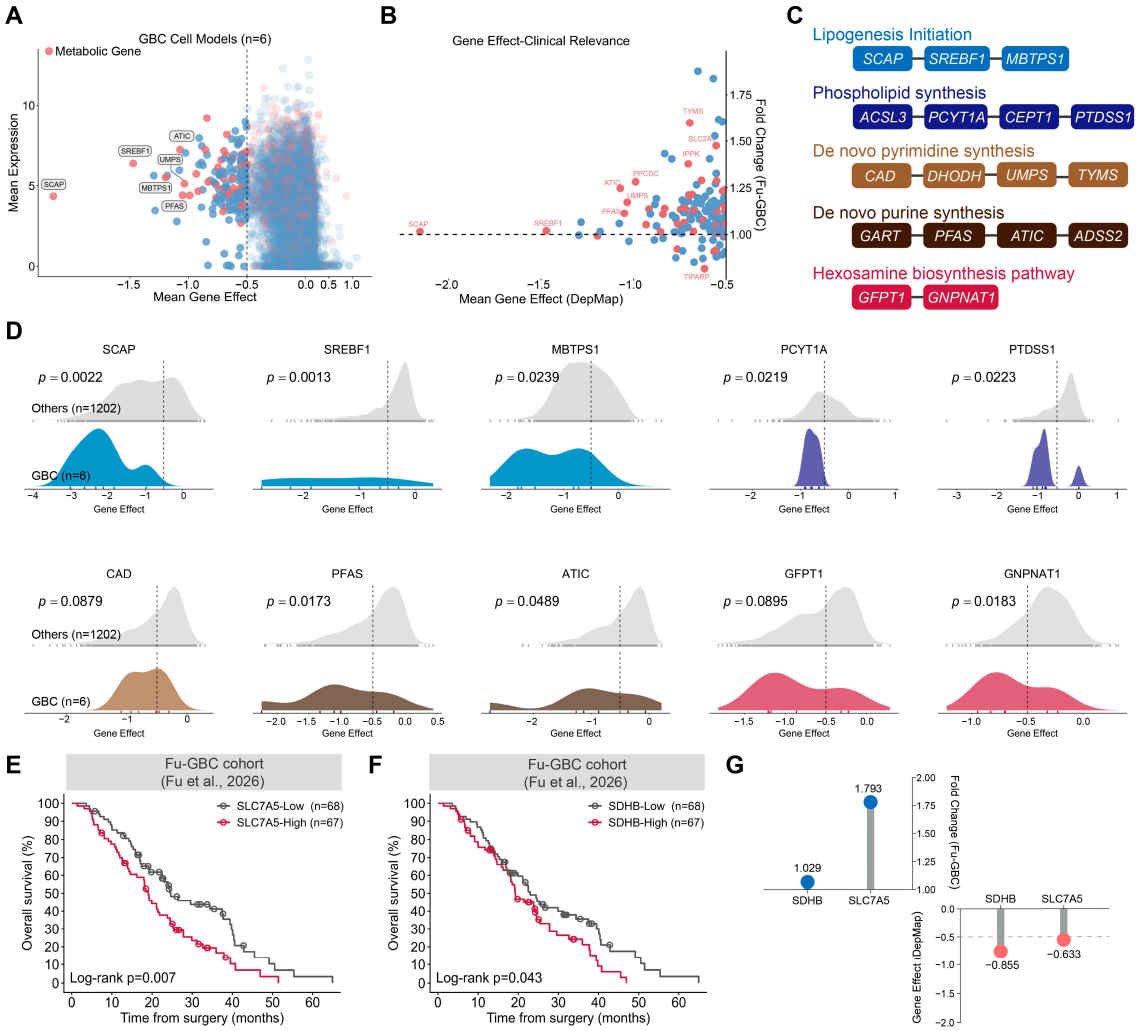


Figure 3. Identification of GBC-selective metabolic dependencies and candidate prognostic biomarkers. (**A**) Mean gene expression versus mean DepMap Gene Effect across GBC cell lines ($n = 6$) for all expressed genes after exclusion of common essential genes, with metabolic genes shown in red and non-metabolic genes in blue; (**B**) cross-referencing functional dependency with tumor expression. Mean DepMap Gene Effect across GBC cell lines (x-axis) is plotted against the tumor-versus-adjacent fold change in the Fu-GBC bulk transcriptomic cohort (y-axis) for cancer-selective genes; (**C**) schematic of GBC-selective metabolic dependencies organized into five metabolic modules; (**D**) density distributions of DepMap Gene Effect scores for representative genes in each metabolic module, comparing GBC cell lines ($n = 6$) with all other cancer cell lines ($n = 1202$); (**E**,**F**) Kaplan–Meier overall survival curves of the Fu-GBC cohort stratified by median expression of *SLC7A5* (**E**) and *SDHB* (**F**) [17]; (**G**) summary of tumor-versus-adjacent fold change (top) and mean DepMap Gene Effect (bottom) for *SDHB* and *SLC7A5* in GBC. Results were analyzed by a two-sided Mann–Whitney U test (**D**) and a log-rank test (**E**,**F**).

Beyond the pathway-level modules, we asked whether individual metabolic genes might serve as standalone prognostic markers in GBC. By cross-referencing all GBC-selective metabolic dependencies (mean Gene Effect < -0.5) with overall survival in the Fu-GBC cohort, we identified *SLC7A5* (also known as *LAT1*) and *SDHB* as candidates with significant adverse prognosis (log-rank $p = 0.007$ and 0.043, respectively; Figure 3E,F). Among these candidates, we focused on *SLC7A5* for further characterization given its three con-

vergent lines of evidence: marked tumor upregulation (FC = 1.79), selective cancer-cell dependency (mean Gene Effect = −0.63) (Figure 3G), and significant adverse prognostic value. As a major neutral amino acid transporter that supplies branched-chain and aromatic amino acids to drive mTORC1 signaling [37,38], *SLC7A5* is closely linked to the dysregulated amino acid transport observed in our metabolomic data. These findings consistently highlight amino acid uptake as a core metabolic vulnerability in GBC. The clinical potential of targeting *SLC7A5* is further supported by recent clinical trial data. A phase 2 randomized, placebo-controlled trial of the first-in-class LAT1-selective inhibitor nanvuranlat (JPH203) was conducted in patients with pre-treated advanced biliary tract cancers including GBC [39]. This trial met its primary endpoint of prolonged progression-free survival, and the therapeutic benefit was most prominent in patients with high LAT1 expression (PFS HR = 0.44, 95% CI 0.23–0.85, $p = 0.01$) [40]. Based on these encouraging results, a global Phase 3 trial (Beacon-BTC; NCT07265674) was initiated in December 2025. Combining functional, transcriptomic and clinical evidence, *SLC7A5* is validated as both a valuable prognostic biomarker and a clinically actionable therapeutic target for GBC.

3.5. Elevated GPD2 Expression Correlates with Poor Prognosis and Tumor Metastasis in GBC

In our metabolomics analysis, Gro3P emerged as the most significantly downregulated metabolite in tumor tissues, whereas its metabolic partner, DHAP, exhibited a marked accumulation. As these two metabolites serve as the essential substrates for the G3PS, this specific metabolic signature led us to focus on the core enzymes governing this process, namely GPD1 and GPD2 (Figure 4A). In the Fu-GBC cohort, *GPD2* was significantly upregulated in GBC, while *GPD1* and *GPD1L* were significantly downregulated (Figure 4B). The uncoupled expression pattern mirrors the reciprocal trends of Gro3P depletion and DHAP accumulation, a pattern observed in several other tumor types and supported by TCGA pan-cancer data across most tumor types (Figures 4C and S1A) [14].

We next validated GPD2 upregulation at the protein level. Western blotting showed higher GPD2 abundance in GBC cell lines than in the immortalized non-tumorigenic gallbladder epithelial cell line L-2F7 (Figure 4D). Consistently, GPD2 protein abundance was increased in paired GBC tumor tissues compared with adjacent nontumor tissues (Figure 4E). Immunohistochemical staining of a GBC tissue microarray further confirmed stronger GPD2 signal in tumor epithelium, with significantly higher immunoreactive scores in tumor regions than in adjacent normal epithelium (Figure 4F,G). In contrast, GPD1 staining did not differ significantly between tumor and adjacent epithelial regions (Figure S1B,C).

To assess the clinical relevance of *GPD2* expression, we evaluated its prognostic value across two independent cohorts. In the Fu-GBC bulk transcriptomic cohort, patients stratified by *GPD2* expression showed a trend toward shorter overall survival in the high-GPD2 group, although the difference approached but did not reach conventional statistical significance at the selected cutoff (log-rank $p = 0.053$; Figure 4H). To corroborate this association in an independent dataset at cell-type-resolved resolution, we computed a per-patient mean of *GPD2* expression across malignant epithelial cells in the Zhou et al. GBC scRNA-seq cohort [18], and stratified patients by this score for Kaplan–Meier analysis. In this cohort, patients with higher epithelial GPD2 expression showed significantly worse overall survival (log-rank $p = 0.033$; Figure 4I), and this prognostic association remained robust across a range of expression cutoffs (Figure S1D). The two datasets exhibited concordant directional effects, together supporting an adverse clinical association of epithelial GPD2 *expression* in GBC.

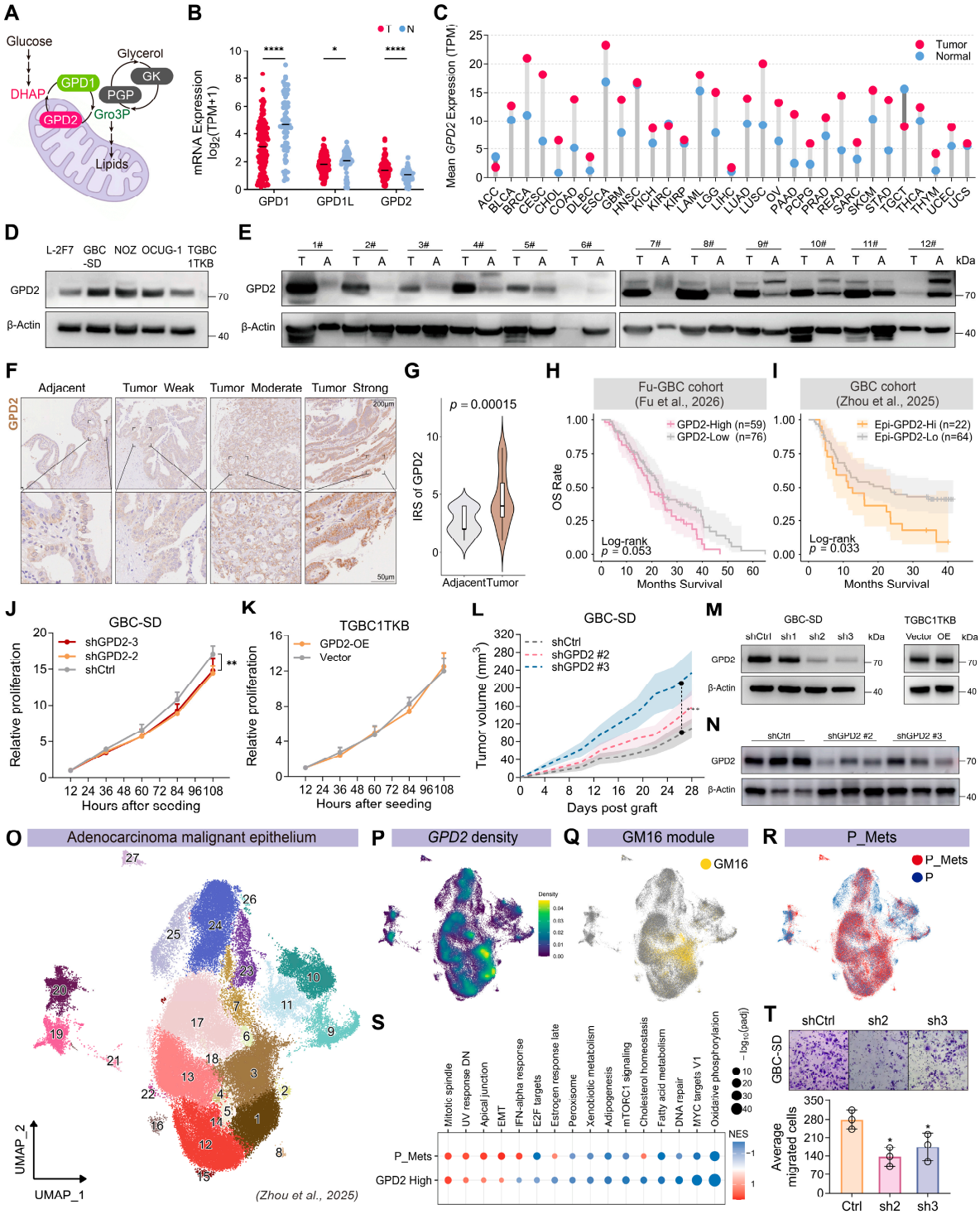


Figure 4. GPD2 expression is associated with a metastasis-related malignant epithelial state, and GPD2 knockdown reduces cell migration in vitro. (**A**) Schematic of the G3PS; (**B**) *GPD1*, *GPD1L* and *GPD2* mRNA expression in tumor (T) versus adjacent non-tumor (N) tissues of the Fu-GBC cohort; (**C**) TCGA pan-cancer *GPD2* expression (TPM) in tumor versus normal tissues; (**D**) Western blot of GPD2 in the immortalized gallbladder epithelial cell line L-2F7 and four GBC cell lines; (**E**) Western blot of GPD2 in 12 paired tumor (T) and adjacent (A) GBC tissues; (**F**,**G**) representative GPD2 immunohistochemistry of adjacent epithelium and tumor regions from a GBC TMA, with tumor staining graded as weak, moderate, or strong (**F**), and IRS quantified in (**G**); (**H**) Kaplan–Meier overall-survival curve of the Fu-GBC cohort stratified by *GPD2* expression [17]; (**I**) Kaplan–Meier overall-survival curve in an independent GBC scRNA-seq cohort ([18]) stratified by epithelial *GPD2* expression [18]; (**J**,**K**) in vitro proliferation of GBC-SD cells transduced with control or *GPD2*-

targeting shRNA (**J**) and TGBC1TKB cells overexpressing *GPD2* (**K**); (**L**) subcutaneous xenograft tumor volume in nude mice bearing GBC-SD shCtrl, sh*GPD2*#2, or sh*GPD2*#3 cells ($n = 6$ per arm); (**M**,**N**) Western blot validation of GPD2 knockdown and overexpression in cell models (**M**) and in excised xenograft tumors (**N**); (**O**–**R**) UMAP of malignant epithelial cells from the scRNA-seq dataset showing 27 subclusters (**O**) [18], *GPD2* expression density (**P**), GM16 (metastasis-associated gene module) overlay (**Q**), and primary tumors with metastasis (P_Mets) versus without (P) (**R**); (**S**) hallmark GSEA dot plot comparing *GPD2*-high versus *GPD2*-low within patients and P_Mets versus P stratifications; (**T**) transwell migration of GBC-SD shCtrl, sh*GPD2*#2, and sh*GPD2*#3 cells: representative images (top) and quantification (bottom). Results were analyzed by a two-sided Mann–Whitney *U* test (**B**,**G**), a log-rank test (**H**,**I**), two-way ANOVA followed by a Dunnett post hoc test (**J**,**L**), two-way ANOVA followed by a Sidak post hoc test (**K**), and one-way ANOVA followed by a Dunnett post hoc test (**T**). * $p < 0.05$; ** $p < 0.01$; *** $p < 0.001$; **** $p < 0.0001$. Data are mean ± SD.

To interrogate the role of GPD2 in GBC, we knocked down (KD) GPD2 in GBC-SD cells using short hairpin RNA (shRNA) and, in parallel, generated GPD2-overexpressing (OE) TGBC1TKB cells (Figures 4M and S1E). Interestingly, we found that GPD2 OE did not influence cell growth in vitro (Figure 4K). In contrast, while GPD2 KD suppressed cell proliferation in vitro (Figure 4J), it paradoxically enhanced the volume of subcutaneous tumors in nude mice (Figure 4L). A subsequent Western blot analysis of the excised tumors confirmed that GPD2 protein levels remained suppressed, suggesting that the accelerated in vivo growth represents a genuine biological consequence of GPD2 deficiency within the complex tumor microenvironment (Figure 4N).

To dissect the cellular heterogeneity underlying this prognostic role of GPD2, we returned to the scRNA-seq dataset. Specifically, we isolated the malignant epithelial cells from primary tumor tissues of patients pathologically diagnosed with adenocarcinoma within the dataset ($n = 75$). Following batch effect correction and data integration, unsupervised clustering resolved the malignant epithelium into 27 distinct cellular subclusters (Figure 4O). Of note, *GPD2* expression was not uniformly distributed among malignant cells but was predominantly restricted to subclusters 1 and 3 (Figure 4O,P). In the original study of this dataset, the authors categorized the malignant epithelium into distinct gene modules using non-negative matrix factorization (NMF). Among these, gene module 16 (GM16) was identified as a patient-shared, highly aggressive module strongly associated with tumor metastasis [18]. Intriguingly, the cellular distribution of *GPD2* strikingly overlapped with that of GM16 (Figure 4Q), with *GPD2* exhibiting its highest expression levels within the GM16 module (Figure S1F). In addition, *GPD2* expression within primary tumor epithelial cells was significantly higher in patients with metastasis than in those without (Figures 4R and S1G). These results associate elevated GPD2 expression with a metastasis-related malignant epithelial transcriptional state and with documented metastasis at the patient level.

Among the 75 patients with malignant epithelial cells from primary tumors in this cohort, 25 patients harbored a sufficient abundance of GPD2-expressing cells to permit a paired pseudobulk comparison (defined as >10 cells in both the GPD2-high and GPD2-low fractions). In parallel, all 75 patients were stratified based on the presence or absence of metastasis. Subsequent gene set enrichment analysis (GSEA) revealed a striking congruence in the altered transcriptomic programs between these two grouping strategies: oxidative phosphorylation emerged as the most significantly downregulated pathway, whereas signatures critical for tumor invasion and metastasis, apical junction and epithelial–mesenchymal transition (EMT), were consistently and markedly upregulated in both contexts (Figure 4S). Consistently, migration assays showed that GPD2 knockdown reduced GBC cell motility in vitro (Figure 4T). These results indicate that the effects of GPD2 knockdown differed between in vitro proliferation and subcutaneous tumor growth. Although GPD2 knockdown reduced the number of migrated cells in vitro, its role in metastatic dissemination

remains to be established. GPD2 is therefore not merely a component of the altered G3PS node but also marks, and may contribute to, a metastasis-associated malignant epithelial state in GBC.

4. Discussion

Here, we provide a systematic view of the metabolic landscape of GBC based on untargeted metabolomic profiling. Integrating these metabolomic data with public transcriptomic cohorts and DepMap CRISPR dependency data, we localized two convergent vulnerabilities—the hexosamine biosynthetic pathway (HBP), where CRISPR dependency on *GFPT1*/*GNPNAT1* coincides with UDP-GlcNAc accumulation and elevated O-GlcNAcylation, and amino acid transport, most notably *SLC7A5*, which is both an adverse prognostic marker and a clinically validated therapeutic target. Beyond these dependencies, we uncovered an uncoupled G3PS. This state is characterized by Gro3P depletion, DHAP accumulation, and reduced expression of *GPD1* and *GPD1L* alongside elevated *GPD2* expression. GPD2 does not support primary tumor growth. Instead, it marks and may promote a metastasis-associated malignant epithelial state that correlates with poor prognosis.

Deregulating cellular metabolism has long been identified as a significant hallmark of cancers, and metabolic addiction provides a compelling rationale for targeting tumor metabolism therapeutically [8,41]. High PKM2 expression has been linked to poor prognosis and enhanced glycolysis in GBC [42,43], in line with the upregulation of glycolytic entry enzymes (*HK1*, *HK2*, *HKDC1*, *GPI*) observed here. We identified *SCAP* and *MBTPS1*—the SREBP-activation machinery that drives transcription of cholesterol-synthesis genes including *HMGCR*—as GBC dependencies [44,45]. This finding aligns with prior evidence that GBC cells rely on de novo cholesterol and mevalonate synthesis. Inhibition of *HMGCR* by statins can suppress tumor growth and increase the sensitivity of GBC cells to cisplatin by disrupting the DNA damage response [46]. A third critical metabolic node is the hexosamine pathway. OGT, a potential therapeutic target in cholangiocarcinoma [47], was upregulated together with increased UDP-GlcNAc levels in GBC. Meanwhile, GFPT1 and GNPNAT1, two enzymes responsible for UDP-GlcNAc synthesis, were confirmed as selective dependencies in GBC cells. Together, these findings identify glycolysis, cholesterol synthesis and the hexosamine pathway as distinct metabolic vulnerabilities for therapeutic intervention in GBC.

The G3PS emerged as a central node in our analysis, because profound Gro3P depletion with reciprocal DHAP accumulation, together with reduced *GPD1*/*GPD1L* and increased *GPD2* expression, pointed to an uncoupled shuttle. Reverse uncoupling of the two arms of the G3PS has been reported in kidney cancer, where cytosolic and mitochondrial GPD activities become functionally imbalanced and support lipid synthesis [13]. Although genetic manipulation of GPD enzymes is known to reshape the Gro3P/DHAP pool [13,24], our metabolomic data capture steady-state pool sizes rather than flux and therefore cannot establish whether GBC cells have genuinely altered the direction or magnitude of G3PS flux. Confirming GPD2-driven Gro3P→DHAP flux in GBC would require isotope tracing. Moreover, whether Gro3P also has non-canonical regulatory roles in tumor pathogenesis beyond serving as a lipid backbone remains unclear. Future studies should also identify the upstream transcriptional regulators that drive GPD1 suppression and GPD2 induction in GBC.

Notably, our data strongly link GPD2 to poor prognosis and metastatic propensity in GBC, but this study is currently constrained by the lack of ideal murine cell lines or spontaneous metastasis models to validate these phenotypes in vivo. Previous studies have demonstrated that alterations in membrane lipid composition dictate metastatic capacity by modulating membrane fluidity [48,49]. Whether the metabolic remodeling of Gro3P and

downstream lipid species governed by GPD2 directly impinges upon membrane biophysical properties is a critical question that demands further detailed investigation.

Untargeted metabolomics provides a broad window into global metabolic alterations and is therefore well suited for mapping the metabolic landscape of underexplored malignancies such as GBC. However, accurate annotation and identification of mass spectrometry peaks remain important bottlenecks. To increase confidence in the key findings, we complemented automated database matching with manual verification of spectral features for selected metabolites. We also applied pathway-based frameworks, including DA score analysis and MSEA, to identify biologically relevant metabolic routes. Nevertheless, unlike transcriptomic gene set enrichment, interpretation of metabolic pathway activity is inherently complex. Inferring pathway activation or suppression solely from metabolite abundance can be misleading, because changes in individual metabolites are rarely determined by a single catalytic reaction [50]. Instead, these metabolic pools could be a result of cellular transport or the cumulative superposition of multiple interconnected pathways. Therefore, we integrated metabolomic profiles with RNA-seq data and used enzyme expression patterns to contextualize metabolite changes and infer potential metabolic rewiring. Future studies using targeted metabolomics and stable isotope tracing will be required to directly quantify metabolic flux and resolve changes in specific metabolite subclasses.

Previous studies have shown that genetic alterations can shape cancer-specific metabolic rewiring programs [51–54]. Accordingly, metabolic profiling based on a limited number of clinical samples or individual cell-line models may be influenced by genotype-specific effects. For example, KRAS mutations have been reported to drive distinct alterations in branched-chain amino acid metabolism across cancer types [55]. In this study, although we integrated clinical metabolomics, transcriptomics, and functional dependency data, future work should more systematically link mutational landscapes with metabolic phenotypes in GBC. Such analyses will be important for determining whether tissue lineage, genomic alterations, or their interaction plays the dominant role in shaping metabolic reprogramming trajectories.

5. Conclusions

In conclusion, by integrating untargeted metabolomics with public transcriptomic cohorts and DepMap CRISPR dependency data, this study delineates the metabolic landscape of gallbladder cancer and identifies two convergent, clinically relevant vulnerabilities: the hexosamine biosynthetic pathway and amino-acid transport, most notably SLC7A5 (LAT1), a prognostic marker and clinically validated therapeutic target. We further define an uncoupled glycerol-3-phosphate shuttle—marked by Gro3P depletion, DHAP accumulation, and reciprocal loss of GPD1/GPD1L with induction of GPD2—in which GPD2, rather than driving primary tumor growth, marks and may promote a metastasis-associated malignant epithelial state that portends poor prognosis. Collectively, these findings advance the understanding of metabolic reprogramming in gallbladder cancer and nominate GPD2, together with the hexosamine and amino-acid-transport nodes, as candidate metabolic targets that warrant further mechanistic and therapeutic investigation.

Supplementary Materials: The following supporting information can be downloaded at: https://www.mdpi.com/article/10.3390/metabo16110904/s1, Figure S1: Pan-cancer GPD1 expression, tumor-tissue staining and single-cell context of GPD2; Table S1: Untargeted metabolomic profiling of gallbladder cancer (GBC) and matched adjacent non-tumor tissues; Table S2: Integrated differential gene expression analysis of GBC transcriptomic datasets; Table S3: Metabolic genes list based on 'Human-GEM'.

Author Contributions: Conceptualization, D.X. and B.Y.; methodology, C.L.C. and K.L.; formal analysis, Y.P., C.L.C. and K.L.; investigation, Y.P., C.L.C., K.L., Z.G., Y.Z. and N.W.; resources, Z.G., Y.Z. and N.W.; data curation, Z.G., Y.Z. and N.W.; writing—original draft preparation, Y.P.; writing—review and editing, D.X. and B.Y.; supervision, D.X. and B.Y.; funding acquisition, Y.Z. and B.Y. All authors have read and agreed to the published version of the manuscript.

Funding: This research was funded by the Joint Funds for the Innovation of Science and Technology, Fujian Province, grant number 2025Y9240, and the National Natural Science Foundation of China, grant number 82273312.

Institutional Review Board Statement: This study was conducted in accordance with the Declaration of Helsinki and approved by the Ethics Committee of Huashan Hospital (Approval No. 2021—Clinical Review—794). The animal experiments were reviewed and approved by the Institutional Animal Care and Use Committee of Huashan Hospital, Fudan University. All animal procedures were performed in accordance with institutional guidelines for the care and use of laboratory animals.

Informed Consent Statement: Informed consent was obtained from all subjects involved in this study. Written informed consent has been obtained from the patients to publish this paper.

Data Availability Statement: The raw peak data from the untargeted metabolomics analysis are provided in Table S1. The differentially expressed gene tables derived from GEO datasets using the Rank-in algorithm are provided in Table S2. The clinical information and RNA-seq data from the Fu-GBC cohort, as well as the scRNA-sequencing data analyzed in this study, are available from the original publications and associated public repositories [17,18]. The cancer dependency data were obtained from the DepMap portal, release DepMap Public 26Q1. The other experimental data and the analysis code generated or used in this study are available from the corresponding author upon reasonable request.

Conflicts of Interest: The authors declare no conflicts of interest.

References

1. Roa, J.C.; García, P.; Kapoor, V.K.; Maithel, S.K.; Javle, M.; Koshiol, J. Gallbladder cancer. *Nat. Rev. Dis. Primers* **2022**, *8*, 69. [CrossRef] [PubMed]
2. Sharma, A.; Sharma, K.L.; Gupta, A.; Yadav, A.; Kumar, A. Gallbladder cancer epidemiology, pathogenesis and molecular genetics: Recent update. *World J. Gastroenterol.* **2017**, *23*, 3978–3998. [CrossRef] [PubMed]
3. Bray, F.; Laversanne, M.; Sung, H.; Ferlay, J.; Siegel, R.L.; Soerjomataram, I.; Jemal, A. Global cancer statistics 2022: GLOBOCAN estimates of incidence and mortality worldwide for 36 cancers in 185 countries. *CA Cancer J. Clin.* **2024**, *74*, 229–263. [CrossRef] [PubMed]
4. National Comprehensive Cancer Network. NCCN Clinical Practice Guidelines in Oncology: Hepatobiliary Cancers. Version 1.2026. 2026. Available online: https://www.nccn.org/guidelines/guidelines-detail?category=1&id=1517 (accessed on 29 May 2026).
5. Giraldo, N.A.; Drill, E.; Satravada, B.A.; Dika, I.E.; Brannon, A.R.; Dermawan, J.; Mohanty, A.; Ozcan, K.; Chakravarty, D.; Benayed, R.; et al. Comprehensive molecular characterization of gallbladder carcinoma and potential targets for intervention. *Clin. Cancer Res.* **2022**, *28*, 5359–5367. [CrossRef] [PubMed]
6. Li, M.; Zhang, Z.; Li, X.; Ye, J.; Wu, X.; Tan, Z.; Liu, C.; Shen, B.; Wang, X.A.; Wu, W.; et al. Whole-exome and targeted gene sequencing of gallbladder carcinoma identifies recurrent mutations in the ErbB pathway. *Nat. Genet.* **2014**, *46*, 872–876. [CrossRef] [PubMed]
7. Song, X.; Hu, Y.; Li, Y.; Shao, R.; Liu, F.; Liu, Y. Overview of current targeted therapy in gallbladder cancer. *Signal Transduct. Target. Ther.* **2020**, *5*, 230. [CrossRef] [PubMed]
8. Hanahan, D. Hallmarks of cancer—Then and now, and beyond. *Cell* **2026**, *189*, 2254–2277. [CrossRef] [PubMed]
9. Kryukov, G.V.; Wilson, F.H.; Ruth, J.R.; Paulk, J.; Tsherniak, A.; Marlow, S.E.; Vazquez, F.; Weir, B.A.; Fitzgerald, M.E.; Tanaka, M.; et al. MTAP deletion confers enhanced dependency on the PRMT5 arginine methyltransferase in cancer cells. *Science* **2016**, *351*, 1214–1218. [CrossRef] [PubMed]
10. Gautam, J.; Wu, J.; Lally, J.S.V.; McNicol, J.D.; Fayyazi, R.; Ahmadi, E.; Oniciu, D.C.; Heaton, S.; Newton, R.S.; Rehal, S.; et al. ACLY inhibition promotes tumour immunity and suppresses liver cancer. *Nature* **2025**, *645*, 507–517. [CrossRef] [PubMed]
11. Wu, S.; Fukumoto, T.; Lin, J.; Nacarelli, T.; Wang, Y.; Ong, D.; Liu, H.; Fatkhutdinov, N.; Zundell, J.A.; Karakashev, S.; et al. Targeting glutamine dependence through GLS1 inhibition suppresses ARID1A-inactivated clear cell ovarian carcinoma. *Nat. Cancer* **2021**, *2*, 189–200. [CrossRef] [PubMed]

12. Boxer, G.E.; Devlin, T.M. Pathways of intracellular hydrogen transport. *Science* **1961**, *134*, 1495–1501. [CrossRef] [PubMed]
13. Yao, C.H.; Park, J.S.; Kurmi, K.; Hu, S.H.; Notarangelo, G.; Crowley, J.; Jacobson, H.; Hui, S.; Sharpe, A.H.; Haigis, M.C. Uncoupled glycerol-3-phosphate shuttle in kidney cancer reveals that cytosolic GPD is essential to support lipid synthesis. *Mol. Cell* **2023**, *83*, 1340–1349.e7. [CrossRef] [PubMed]
14. Oh, S.; Mai, X.L.; Kim, J.; de Guzman, A.C.V.; Lee, J.Y.; Park, S. Glycerol 3-phosphate dehydrogenases (1 and 2) in cancer and other diseases. *Exp. Mol. Med.* **2024**, *56*, 1066–1079. [CrossRef] [PubMed]
15. Wang, Z.; Wang, S.; Jia, Z.; Zhao, Y.; Yang, M.; Yan, W.; Chen, T.; Xiang, D.; Shao, R.; Liu, Y. Establishment and characterization of an immortalized epithelial cell line from human gallbladder. *Front. Oncol.* **2022**, *12*, 994087. [CrossRef] [PubMed]
16. Tang, K.; Ji, X.; Zhou, M.; Deng, Z.; Huang, Y.; Zheng, G.; Cao, Z. Rank-in: Enabling integrative analysis across microarray and RNA-seq for cancer. *Nucleic Acids Res.* **2021**, *49*, e99. [CrossRef] [PubMed]
17. Fu, Z.; Song, Y.; Liu, F.; Chen, L.; Cai, S.; Cui, P.; Wang, G.; Xie, W.; Zhang, S.; Ding, L.; et al. Integrative proteogenomic analysis provides molecular insights and clinical significance in gallbladder cancer. *Cancer Cell* **2026**, *44*, 405–423.e13. [CrossRef] [PubMed]
18. Zhou, T.; Wu, Y.; Li, S.; Qiu, X.; Liu, E.; Xie, Z.; Shi, X.; Zhang, Y.; Ma, G.; Guo, W.; et al. Multi-omic analysis of gallbladder cancer identifies distinct tumor microenvironments associated with disease progression. *Nat. Genet.* **2025**, *57*, 1935–1949. [CrossRef] [PubMed]
19. Hakimi, A.A.; Reznik, E.; Lee, C.H.; Creighton, C.J.; Brannon, A.R.; Luna, A.; Aksoy, B.A.; Liu, E.M.; Shen, R.; Lee, W.; et al. An integrated metabolic atlas of clear cell renal cell carcinoma. *Cancer Cell* **2016**, *29*, 104–116. [CrossRef] [PubMed]
20. Parker, S.J.; Amendola, C.R.; Hollinshead, K.E.R.; Yu, Q.; Yamamoto, K.; Encarnación-Rosado, J.; Rose, R.E.; LaRue, M.M.; Sohn, A.S.W.; Biancur, D.E.; et al. Selective alanine transporter utilization creates a targetable metabolic niche in pancreatic cancer. *Cancer Discov.* **2020**, *10*, 1018–1037. [CrossRef] [PubMed]
21. Yang, F.; Xiao, Y.; Ding, J.H.; Jin, X.; Ma, D.; Li, D.Q.; Shi, J.X.; Huang, W.; Wang, Y.P.; Jiang, Y.Z.; et al. Ferroptosis heterogeneity in triple-negative breast cancer reveals an innovative immunotherapy combination strategy. *Cell Metab.* **2023**, *35*, 84–100.e8. [CrossRef] [PubMed]
22. Locasale, J.W. Serine, glycine and one-carbon units: Cancer metabolism in full circle. *Nat. Rev. Cancer* **2013**, *13*, 572–583. [CrossRef] [PubMed]
23. Combs, J.A.; DeNicola, G.M. The non-essential amino acid cysteine becomes essential for tumor proliferation and survival. *Cancers* **2019**, *11*, 678. [CrossRef] [PubMed]
24. Oh, S.; Jo, S.; Bajzikova, M.; Kim, H.S.; Dao, T.T.P.; Rohlena, J.; Kim, J.M.; Neuzil, J.; Park, S. Non-bioenergetic roles of mitochondrial GPD2 promote tumor progression. *Theranostics* **2023**, *13*, 438–457. [CrossRef] [PubMed]
25. Nguyen, T.H.; Mai, X.L.; Nguyen, T.T.M.; Nam, H.; Park, S.; Lee, J.Y. Epigenetically-controlled CEBPB regulates kidney cancer tumorigenesis via GPD1L-mediated ether lipid synthesis. *Cell Death Dis.* **2026**, *17*, 175. [CrossRef] [PubMed]
26. Wu, S.; Mao, C.; Kondiparthi, L.; Poyurovsky, M.V.; Olszewski, K.; Gan, B. A ferroptosis defense mechanism mediated by glycerol-3-phosphate dehydrogenase 2 in mitochondria. *Proc. Natl. Acad. Sci. USA* **2022**, *119*, e2121987119. [CrossRef] [PubMed]
27. Zou, Y.; Henry, W.S.; Ricq, E.L.; Graham, E.T.; Phadnis, V.V.; Maretich, P.; Paradkar, S.; Boehnke, N.; Deik, A.A.; Reinhardt, F.; et al. Plasticity of ether lipids promotes ferroptosis susceptibility and evasion. *Nature* **2020**, *585*, 603–608. [CrossRef] [PubMed]
28. Werner, E.R.; Keller, M.A.; Sailer, S.; Lackner, K.; Koch, J.; Hermann, M.; Coassin, S.; Golderer, G.; Werner-Felmayer, G.; Zoeller, R.A.; et al. The TMEM189 gene encodes plasmanylethanolamine desaturase which introduces the characteristic vinyl ether double bond into plasmalogens. *Proc. Natl. Acad. Sci. USA* **2020**, *117*, 7792–7798. [CrossRef] [PubMed]
29. Ferrer, C.M.; Sodi, V.L.; Reginato, M.J. O-GlcNAcylation in cancer biology: Linking metabolism and signaling. *J. Mol. Biol.* **2016**, *428*, 3282–3294. [CrossRef] [PubMed]
30. Verrey, F.; Closs, E.I.; Wagner, C.A.; Palacin, M.; Endou, H.; Kanai, Y. CATs and HATs: The SLC7 family of amino acid transporters. *Pflug. Arch.* **2004**, *447*, 532–542. [CrossRef] [PubMed]
31. Casero, R.A., Jr.; Murray Stewart, T.; Pegg, A.E. Polyamine metabolism and cancer: Treatments, challenges and opportunities. *Nat. Rev. Cancer* **2018**, *18*, 681–695. [CrossRef] [PubMed]
32. van Veen, S.; Martin, S.; Van den Haute, C.; Benoy, V.; Lyons, J.; Vanhoutte, R.; Kahler, J.P.; Decuypere, J.P.; Gelders, G.; Lambie, E.; et al. ATP13A2 deficiency disrupts lysosomal polyamine export. *Nature* **2020**, *578*, 419–424. [CrossRef] [PubMed]
33. Pegg, A.E. Spermidine/spermine-N^1-acetyltransferase: A key metabolic regulator. *Am. J. Physiol. Endocrinol. Metab.* **2008**, *294*, E995–E1010. [CrossRef] [PubMed]
34. Robinson, J.L.; Kocabaş, P.; Wang, H.; Cholley, P.E.; Cook, D.; Nilsson, A.; Anton, M.; Ferreira, R.; Domenzain, I.; Billa, V.; et al. An atlas of human metabolism. *Sci. Signal.* **2020**, *13*, eaaz1482. [CrossRef] [PubMed]
35. Solimini, N.L.; Luo, J.; Elledge, S.J. Non-oncogene addiction and the stress phenotype of cancer cells. *Cell* **2007**, *130*, 986–988. [CrossRef] [PubMed]
36. Vander Heiden, M.G.; DeBerardinis, R.J. Understanding the intersections between metabolism and cancer biology. *Cell* **2017**, *168*, 657–669. [CrossRef] [PubMed]

37. Nicklin, P.; Bergman, P.; Zhang, B.; Triantafellow, E.; Wang, H.; Nyfeler, B.; Yang, H.; Hild, M.; Kung, C.; Wilson, C.; et al. Bidirectional transport of amino acids regulates mTOR and autophagy. *Cell* **2009**, *136*, 521–534. [CrossRef] [PubMed]
38. Häfliger, P.; Charles, R.P. The L-type amino acid transporter LAT1—An emerging target in cancer. *Int. J. Mol. Sci.* **2019**, *20*, 2428. [CrossRef] [PubMed]
39. Furuse, J.; Ikeda, M.; Ueno, M.; Furukawa, M.; Morizane, C.; Takehara, T.; Nishina, T.; Todaka, A.; Okano, N.; Hara, K.; et al. A phase II placebo-controlled study of the effect and safety of nanvuranlat in patients with advanced biliary tract cancers previously treated by systemic chemotherapy. *Clin. Cancer Res.* **2024**, *30*, 3990–3995. [CrossRef] [PubMed]
40. Ikeda, M.; Ueno, M.; Furukawa, M.; Morizane, C.; Takehara, T.; Nishina, T.; Todaka, A.; Okano, N.; Hara, K.; Nakai, Y.; et al. Subgroup analysis of double-blind, placebo-controlled Ph. 2 study of nanvuranlat in treatment of pre-treated, advanced, refractory biliary tract cancer (BTC): Patients with high LAT1 expression and response to nanvuranlat. *J. Clin. Oncol.* **2023**, *41*, 4011. [CrossRef]
41. Stine, Z.E.; Schug, Z.T.; Salvino, J.M.; Dang, C.V. Targeting cancer metabolism in the era of precision oncology. *Nat. Rev. Drug Discov.* **2022**, *21*, 141–162. [CrossRef] [PubMed]
42. Lu, W.; Cao, Y.; Zhang, Y.; Li, S.; Gao, J.; Wang, X.A.; Mu, J.; Hu, Y.P.; Jiang, L.; Dong, P.; et al. Up-regulation of PKM2 promote malignancy and related to adverse prognostic risk factor in human gallbladder cancer. *Sci. Rep.* **2016**, *6*, 26351. [CrossRef] [PubMed]
43. He, Z.; Zhong, Y.; Lv, T.; Wang, J.; Jin, Y.; Li, F.; Hu, H. PP4R1 promotes glycolysis and gallbladder cancer progression through facilitating ERK1/2 mediated PKM2 nuclear translocation. *Cancer Lett.* **2024**, *586*, 216677. [CrossRef] [PubMed]
44. Brown, M.S.; Goldstein, J.L. The SREBP pathway: Regulation of cholesterol metabolism by proteolysis of a membrane-bound transcription factor. *Cell* **1997**, *89*, 331–340. [CrossRef] [PubMed]
45. Brown, M.S.; Goldstein, J.L. A proteolytic pathway that controls the cholesterol content of membranes, cells, and blood. *Proc. Natl. Acad. Sci. USA* **1999**, *96*, 11041–11048. [CrossRef] [PubMed]
46. Zhang, Y.; Liu, Y.; Duan, J.; Wang, H.; Zhang, Y.; Qiao, K.; Wang, J. Cholesterol depletion sensitizes gallbladder cancer to cisplatin by impairing DNA damage response. *Cell Cycle* **2019**, *18*, 3337–3350. [CrossRef] [PubMed]
47. Charoensuksai, P.; Jirawatnotai, S. O-GlcNAcylation as an emerging molecular target for cholangiocarcinoma therapy (Review). *Oncol. Rep.* **2025**, *54*, 119. [CrossRef] [PubMed]
48. Zhao, W.; Prijic, S.; Urban, B.C.; Tisza, M.J.; Zuo, Y.; Li, L.; Tan, Z.; Chen, X.; Mani, S.A.; Chang, J.T. Candidate antimetastasis drugs suppress the metastatic capacity of breast cancer cells by reducing membrane fluidity. *Cancer Res.* **2016**, *76*, 2037–2049. [CrossRef] [PubMed]
49. Wang, Y.; Hu, M.; Cao, J.; Wang, F.; Han, J.R.; Wu, T.W.; Li, L.; Yu, J.; Fan, Y.; Xie, G.; et al. ACSL4 and polyunsaturated lipids support metastatic extravasation and colonization. *Cell* **2025**, *188*, 412–429.e27. [CrossRef] [PubMed]
50. Lee, K.S.; Su, X.; Huan, T. Metabolites are not genes—Avoiding the misuse of pathway analysis in metabolomics. *Nat. Metab.* **2025**, *7*, 858–861. [CrossRef] [PubMed]
51. Ma, Q.; Zhang, W.; Wu, K.; Shi, L. The roles of KRAS in cancer metabolism, tumor microenvironment and clinical therapy. *Mol. Cancer* **2025**, *24*, 14. [CrossRef] [PubMed]
52. Maddocks, O.D.; Berkers, C.R.; Mason, S.M.; Zheng, L.; Blyth, K.; Gottlieb, E.; Vousden, K.H. Serine starvation induces stress and p53-dependent metabolic remodelling in cancer cells. *Nature* **2013**, *493*, 542–546. [CrossRef] [PubMed]
53. Son, J.; Lyssiotis, C.A.; Ying, H.; Wang, X.; Hua, S.; Ligorio, M.; Perera, R.M.; Ferrone, C.R.; Mullarky, E.; Shyh-Chang, N.; et al. Glutamine supports pancreatic cancer growth through a KRAS-regulated metabolic pathway. *Nature* **2013**, *496*, 101–105. [CrossRef] [PubMed]
54. Vousden, K.H.; Ryan, K.M. p53 and metabolism. *Nat. Rev. Cancer* **2009**, *9*, 691–700. [CrossRef] [PubMed]
55. Mayers, J.R.; Torrence, M.E.; Danai, L.V.; Papagiannakopoulos, T.; Davidson, S.M.; Bauer, M.R.; Lau, A.N.; Ji, B.W.; Dixit, P.D.; Hosios, A.M.; et al. Tissue of origin dictates branched-chain amino acid metabolism in mutant Kras-driven cancers. *Science* **2016**, *353*, 1161–1165. [CrossRef] [PubMed]

Disclaimer/Publisher's Note: The statements, opinions and data contained in all publications are solely those of the individual author(s) and contributor(s) and not of MDPI and/or the editor(s). MDPI and/or the editor(s) disclaim responsibility for any injury to people or property resulting from any ideas, methods, instructions or products referred to in the content.